

## Article

# Highly Dispersed Nickel Nanoparticles on Hierarchically Ordered Macroporous Al<sub>2</sub>O<sub>3</sub> and Its Catalytic Performance for Steam Reforming of 1-Methyl Naphthalene

Lien Thi Do <sup>1</sup>, Huy Nguyen-Phu <sup>2</sup> , Ngoc Nhiem Pham <sup>3</sup>, Dong Hwi Jeong <sup>3</sup> and Eun Woo Shin <sup>3,\*</sup> 

<sup>1</sup> Faculty of Biotechnology, Chemistry and Environmental Engineering, Phenikaa University, Hanoi 10000, Vietnam

<sup>2</sup> Department of Chemical and Biomolecular Engineering, Seoul National University of Science and Technology, Seoul 01811, Republic of Korea

<sup>3</sup> School of Chemical Engineering, University of Ulsan Daehakro 93, Nam-gu, Ulsan 44610, Republic of Korea

\* Correspondence: ewshin@ulsan.ac.kr; Tel.: +82-52-259-2253

**Abstract:** In this study, we investigate the effect of a hierarchically ordered macroporous structure of alumina support on the steam reforming of 1-methyl naphthalene with mesoporous alumina-supported nickel and potassium (xK/Ni–MeAl), and macroporous alumina-supported nickel and potassium (xK/Ni–MaAl) catalysts. Hierarchically ordered macroporosity in Al<sub>2</sub>O<sub>3</sub> supports plays an important role in maintaining the high Ni dispersion through multiple interactions in Ni–K over AlO<sub>4</sub> tetrahedra in alumina. This, in turn, improves the catalytic performance of steam reforming, including high gas yields, turnover frequency for hydrogen production, and 1-methyl naphthalene conversion. At high K content, the Ni active sites over xK/Ni–MeAl catalysts significantly decrease, resulting in almost zero steam reforming rate in the reaction test. Conversely, the potassium–alumina interaction in xK/Ni–MaAl catalysts not only diminishes the formation of the inactive nickel aluminate phase but also maintains the highly dispersed Ni active sites, resulting in a high steam reforming rate.

**Keywords:** steam reforming; multiple metal support interactions; hierarchically ordered macroporosity; nickel dispersion; steam cracking



**Citation:** Do, L.T.; Nguyen-Phu, H.; Pham, N.N.; Jeong, D.H.; Shin, E.W. Highly Dispersed Nickel Nanoparticles on Hierarchically Ordered Macroporous Al<sub>2</sub>O<sub>3</sub> and Its Catalytic Performance for Steam Reforming of 1-Methyl Naphthalene. *Catalysts* **2022**, *12*, 1542. <https://doi.org/10.3390/catal12121542>

Academic Editors: Dezhi Han, Wentai Wang and Ning Han

Received: 26 October 2022

Accepted: 26 November 2022

Published: 30 November 2022

**Publisher's Note:** MDPI stays neutral with regard to jurisdictional claims in published maps and institutional affiliations.



**Copyright:** © 2022 by the authors. Licensee MDPI, Basel, Switzerland. This article is an open access article distributed under the terms and conditions of the Creative Commons Attribution (CC BY) license (<https://creativecommons.org/licenses/by/4.0/>).

## 1. Introduction

Climate change and future fossil fuel limitations will, in a short period of time, result in a shift in the world's energy consumption from fossil fuels to renewable energy sources that are environmentally friendly and naturally sustainable. Biomass is one such renewable source for producing biogas and liquid biofuel [1]. Recent studies have attempted to develop measures for biomass conversion to energy and fuel, such as biomass gasification, biomass liquefaction, and biomass pyrolysis [2–8]. Of the various methods for biomass conversion, biomass gasification has received the most attention because of its higher energy recovery and head capacity [9]. However, the high level of tar generated during biomass gasification poses serious operational problems for downstream processes. The condensation of heavy tars and the crystallization of light tars (e.g., naphthalene) cause fouling at low temperatures (<350 °C) on gas engines and control valves. Therefore, most biomass gasification products require the removal of dust and tar before employing them in subsequent processes. Therefore, tar conversion is a vital aspect in successfully applying biomass gasification for energy production.

Steam reforming is currently used for removing tars generated during biomass gasification because such tars produce syngas and hydrogen fuels [10–13]. However, raw tar from the biomass gasifier includes not only a complex mixture of condensable hydrocarbons but also various contaminants, including particulates, nitrogen-containing compounds, and sulfur. Understanding the fundamental relation between active sites on

the catalyst, molecular structures, and raw tar conversion during steam reforming can be difficult. Therefore, representative tar compounds that possess aromatic rings and oxygen-containing aromatic hydrocarbons, such as benzene, toluene, naphthalene, and phenol, were chosen to investigate the removal of tars via steam reforming [14]. Metal-containing catalysts—Rh, Ni, and Co—have been developed for steam reforming of biomass tar. Of these, Ni-containing catalysts are known as commercial industrial catalysts for steam reforming because they are competitive in terms of cost and performance efficiency [13,15]. In past research, Ni/Al<sub>2</sub>O<sub>3</sub> catalysts have been widely used for steam reforming because of their high conversion and potential hydrogen yield [16–21]. When these catalysts are used, Ni dispersion or the Ni particle size on alumina supports has directly affected catalytic performance in steam reforming. High Ni dispersion resisted coke generation during steam reforming [22] and minimized the formation of Ni clusters even at high temperatures because the mobility of Ni particles was weaker when the distance between two nickel particles increased [23]. The Ni dispersion on Ni/Al<sub>2</sub>O<sub>3</sub> catalysts can be improved by modifying the catalyst surface through the doping of promoters or via changes in alumina morphology and structure [24,25].

Modifying the surface of Ni/Al<sub>2</sub>O<sub>3</sub> catalysts by adding potassium (K) influences catalytic activity and selectivity during steam reforming [20,21,26–28]. The donation of an electron from K to Ni increases the electron density of the Ni cluster, which corresponds to higher Ni activity and a lower barrier of dissociative methane in steam–methane reforming [20]. Another study also reports that the K dopant adjusts the surface acidity of the support and modifies the Ni active sites in mixed active phase Ni<sup>0</sup>/Ni<sup>2+</sup>, which not only enhances both steam reforming and gasification reactions, but also suppresses the methanation process [26]. However, we have yet to fully understand the K-addition effect on steam reforming over Ni/Al<sub>2</sub>O<sub>3</sub> catalysts. Additionally, many opposing views exist on this matter, and many cite its negative effects. The addition of alkali metals also decreases the steam reforming rate and significantly promotes the nickel sintering rate under high-pressure conditions [21,27,28]. For this reason, in this research, different K contents were impregnated onto Ni–alumina supports for investigation of the effect of not only the K–alumina interaction but also the K–Ni interaction on steam reforming.

The effect of macro/mesoporous supports has also been investigated in recent years. Papers report that macro/mesopore channels reduce the length of mesopore channels in conventional mesoporous supports and improve the diffusion of reactants to active sites on the catalyst surface. As a result, increased accessibility to active sites dramatically improves catalytic performance [29–33]. However, even though understanding the catalytic behavior and properties related to the macro/mesoporous structure in the supports for steam reforming is essential; to date, there have been no reports regarding the influence of macro/mesoporosity in Ni/Al<sub>2</sub>O<sub>3</sub> catalysts on the formation of active sites over catalysts, and no explanation on how changes in active site formation affect catalyst performance.

In this study, we prepared both hierarchically ordered macroporous alumina (MaAl) and mesoporous alumina (MeAl) as supports for Ni/Al<sub>2</sub>O<sub>3</sub> catalysts for steam reforming of tar and employed them to further understand the effect of hierarchically ordered macro/mesoporosity of alumina on the steam reforming process. To observe this reaction, 1-methyl naphthalene (1-MN) was chosen as a model tar compound. Furthermore, the multiple interactions between Ni, K, and alumina supports with macro/mesoporosity were explored. The formation of Ni active sites for steam reforming and catalytic behavior over Ni/Al<sub>2</sub>O<sub>3</sub> catalysts were described according to the different multiple interactions between Ni–K–alumina based on hierarchically ordered macro/mesoporosity.

## 2. Results and Discussion

### 2.1. Catalytic Characteristics

A hierarchically macroporous structure was observed on the surface of the reduced xK/Ni–MaAl catalysts in the SEM (see Figures 1 and S1) and TEM images (see Figure S2). Interestingly, no differences were observed in the macroporous morphology when potas-

sium was added to the MaAl, and triangular-shaped particles in the SEM images became more abundant on the surface of MeAl when the potassium content increased from 0% to 2% in the  $x\text{K}/\text{Ni}-\text{MeAl}$  catalysts (Figure 1a–d). The appearance of triangular-shaped particles was a result of the interaction between K and  $\text{Al}_2\text{O}_3$  after calcining potassium nitrate at 600 °C, which could be observed by TEM and TEM-EDS mapping images (Figures S3 and S4). However, this triangle-like K- $\text{Al}_2\text{O}_3$  was barely observed in the  $x\text{K}/\text{Ni}-\text{MaAl}$  catalysts, which indicates a different K and  $\text{Al}_2\text{O}_3$  interaction in the pores of the MaAl support. The green spots in the TEM-EDS mapping images (Figure 2) were characterized as Ni metal on the supports, indicating that the Ni particle size in the  $x\text{K}/\text{Ni}-\text{MaAl}$  catalysts ( $\sim 5.1$  nm for  $x = 0.5$ ) was smaller than that in the  $x\text{K}/\text{Ni}-\text{MeAl}$  catalysts ( $\sim 15.8$  nm for  $x = 0.5$ ), and this indicated that Ni was better dispersed on the hierarchically ordered MaAl support than on the MeAl support.

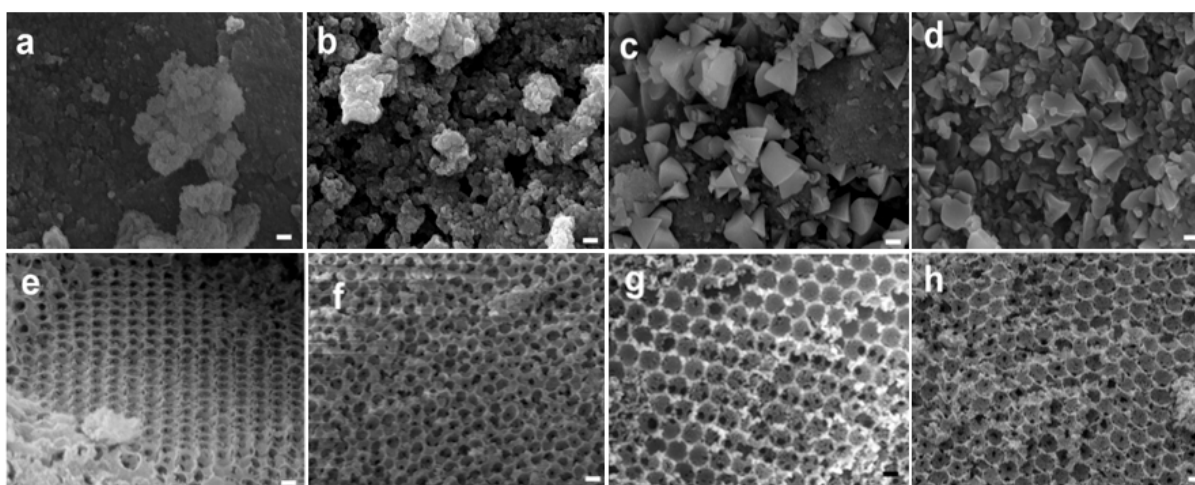


**Figure 1.** The SEM images of (a) MeAl, (b) Ni-MeAl, (c) 0.5K/Ni-MeAl, (d) 2K/Ni-MeAl, (e) MaAl, (f) Ni-MaAl, (g) 0.5K/Ni-MaAl, and (h) 2K/Ni-MaAl. (Scale bar = 200 nm).

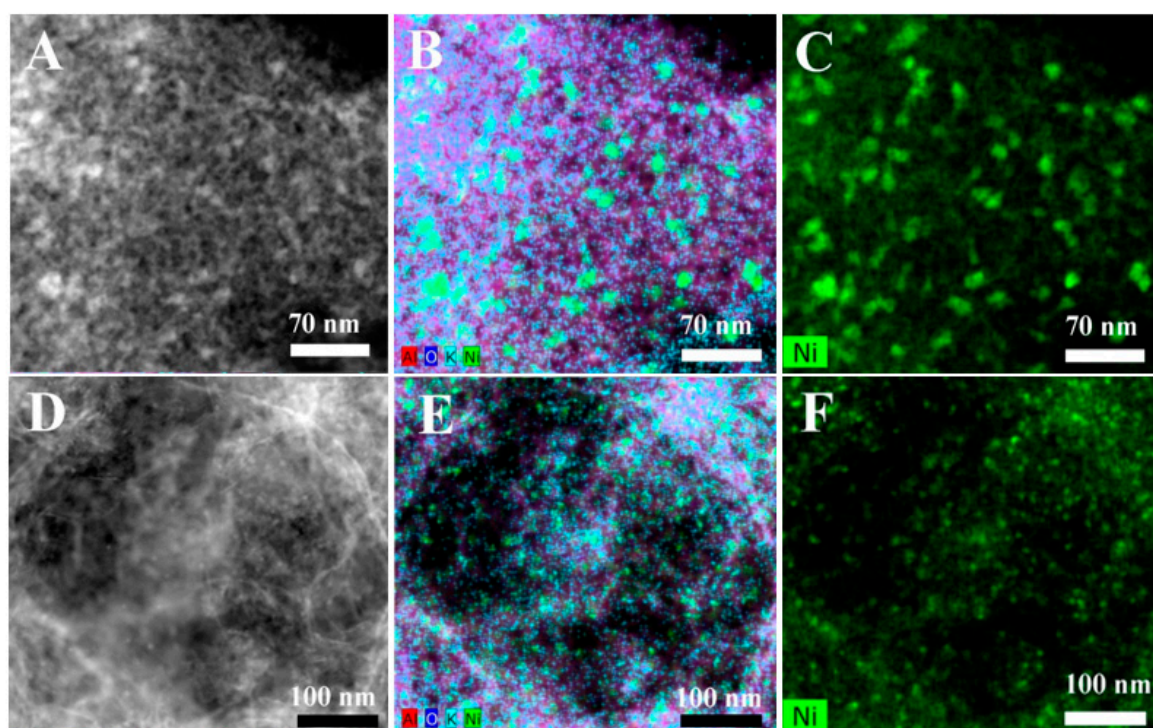


**Figure 2.** The TEM and TEM-EDS mapping images of (A–C) 0.5K/Ni-MeAl and (D–F) 0.5K/Ni-MaAl.

The nitrogen adsorption and desorption isotherm curves and the pore-size distributions of both xK/Ni–MeAl and xK/Ni–MaAl catalysts are shown in Figure 3. The BET surface area of the xK/Ni–MeAl catalysts decreased significantly when Ni and K were added, whereas the addition of Ni and K slowly decreased the BET surface area of the xK/Ni–MaAl catalysts (Figure 3A and Table 1). Shown in Figure 3B, the mesopore sizes in xK/Ni–MaAl (2–35 nm) were larger than those in xK/Ni–MeAl (2–8 nm). The significant decrease in pore volume and size after the addition of Ni and K onto the MeAl supports (Table 1) implied either pore blocking by the large-sized Ni particles or a new phase between K and Al<sub>2</sub>O<sub>3</sub>. Even though this phenomenon could also occur in xK/Ni–MaAl, the Ni and K addition on the macro/mesoporous channels and multiple interactions between Ni–K–Al<sub>2</sub>O<sub>3</sub> supports induced a smaller Ni size and a slight decline in the pore volume and average pore size of the MaAl support (Table 1).

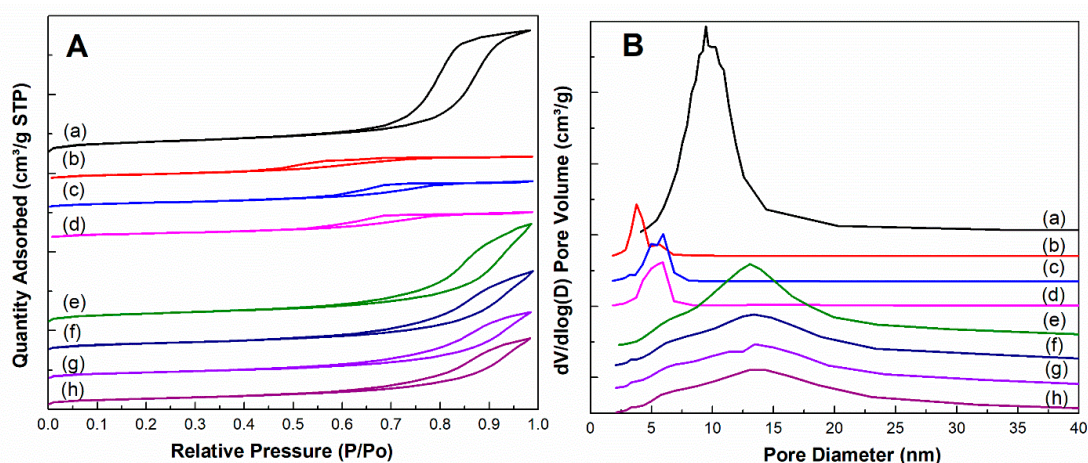


**Figure 3.** Nitrogen adsorption–desorption isotherm curves (A) and pore-size distribution (B) of (a) MeAl, (b) Ni–MeAl, (c) 0.5K/Ni–MeAl, (d) 2K/Ni–MeAl, (e) MaAl, (f) Ni–MaAl, (g) 0.5K/Ni–MaAl, and (h) 2K/Ni–MaAl.

**Table 1.** Physicochemical properties of the prepared catalysts.

Catalysts	Surface Area (m <sup>2</sup> /g)	Pore Size (nm)	Pore Volume (cm <sup>3</sup> /g)	Ni Size (nm) TEM/XRD	NiO/Ni Peak Area Ratio (XRD)	Acidic Sites (mmol/g)	Ni Sites from H <sub>2</sub> -TPR (mmol/g)
MeAl	314.2	9.5	1.24	-	-	1.359	-
Ni–MeAl	177.7	4.0	0.25	11.17/4.7	Only Ni	0.586	0.012
0.5K/Ni–MeAl	172.0	5.1	0.29	15.8/8.2	0.29	0.419	0.008
2K/Ni–MeAl	168.8	5.1	0.29	46.8/7.9	Only NiO	0.370	0.006
MaAl	266.2	11.5	1.00	-	-	2.033	-
Ni–MaAl	221.5	10.8	0.81	2.8/1.8	Only Ni	0.773	0.017
0.5K/Ni–MaAl	202.1	10.2	0.69	5.1/2.1	0.19	0.527	0.017
2K/Ni–MaAl	199.5	10.4	0.68	6.7/2.1	0.31	0.518	0.014

The reducibility of the calcined catalysts was measured from 50 °C to 900 °C by H<sub>2</sub>-TPR experiments, and the H<sub>2</sub>-TPR profiles are shown in Figure 4. In the H<sub>2</sub>-TPR profiles, a primary broad reduction peak from 400 °C to 800 °C was assigned to the reduction of nickel oxide or NiAl<sub>2</sub>O<sub>4</sub> on the surface of Al<sub>2</sub>O<sub>3</sub> [34–36]. The large peak area of reduced NiO for the xK/Ni–MaAl catalysts implied a high number of Ni metallic sites (Table 1). Interestingly, the shoulder peak at 600 °C only appeared in xK/Ni–MaAl catalysts, confirming the smaller size of NiO on the surface, while the main peak at around 720 °C represented the reduction of NiAl<sub>2</sub>O<sub>4</sub> [37]. In addition, the peak shift of NiO reduction to a higher temperature after K addition (both MeAl and MaAl) indicated the oligomerization of NiO particles.

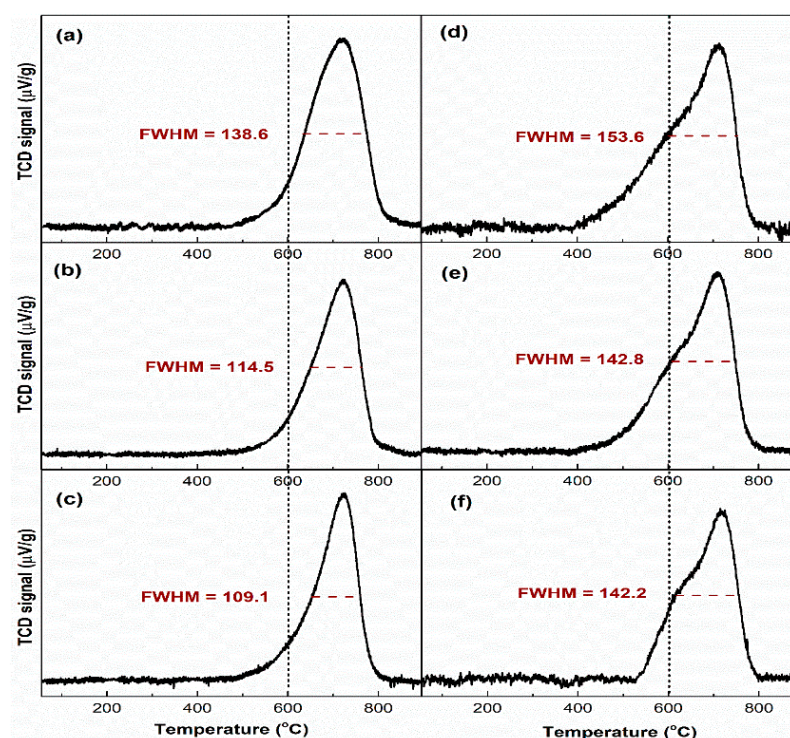


**Figure 4.** The H<sub>2</sub>-TPR profiles of (a) NiO–MeAl, (b) 0.5K/NiO–MeAl, (c) 2K/NiO–MeAl, (d) NiO–MaAl, (e) 0.5K/NiO–MaAl, and (f) 2K/NiO–MaAl.

Figure 5 provides the XRD patterns of both mesoporous and macroporous catalysts after calcining in air and subsequent reduction in hydrogen at 600 °C. For calcined catalysts (Figure 5A), following Ni impregnation onto the alumina supports, a peak shift occurred in the alumina XRD patterns, from  $2\theta = 45.8^\circ$ ,  $60.5^\circ$ , and  $66.8^\circ$  to  $2\theta = 45.4^\circ$ ,  $59.9^\circ$ , and  $66.3^\circ$  (gamma aluminum oxide, JCPDS Card No. 10-0425, space group Fd3m). This indicated the formation of a new surface nickel aluminate-like spinel phase (NiAl<sub>2</sub>O<sub>4</sub>) as a result of the interaction between Ni<sup>2+</sup> ions and Al<sub>2</sub>O<sub>3</sub> at the interface [38–41]. A dramatic decrease in Al<sub>2</sub>O<sub>3</sub> acidity following the addition of Ni also suggested the substitution of Ni<sup>2+</sup> ions inside the tetrahedral interstice of Al<sup>3+</sup> in Al<sub>2</sub>O<sub>3</sub> (Table 1). In previous research, Al<sup>3+</sup> ions have been shown to occupy octahedral and tetrahedral interstices in the  $\gamma$ -Al<sub>2</sub>O<sub>3</sub> crystal, where they are surrounded by densely packed oxygen ions [42,43]. On the basis of the molecular orbital energies, Al<sup>3+</sup> ions in the tetrahedral interstice serve as stronger electron acceptors than those in the octahedral interstice, leading to higher acidity of the tetrahedral surface Al site. The decrease in the tetrahedral Al site by Ni substitution caused the loss of acidity on the alumina surface. Additionally, in comparison to MeAl, MaAl possessed higher acidity (Lewis acid) and the peak at  $2\theta = 31.7^\circ$ , representing the reflection plane with aluminum in tetrahedral position [44,45], only observed clearly for MaAl (Figures 5 and S5), demonstrated a high portion of AlO<sub>4</sub> in the structure of MaAl. This might increase the interaction between Ni and MaAl, rather than MeAl support. After reduction, three phases of Ni (metallic Ni, nickel oxide, nickel aluminate) can be seen in Figure 5B. The existence of a characteristic XRD peak for nickel oxide at  $2\theta = 43.4^\circ$  (JCPDS No. 47-1049, space group Fm3m) for the reduced catalysts indicated that NiO was not completely reduced in hydrogen at 600 °C for 2 h [38]. It is notable that the peak at  $2\theta = 43.4^\circ$  for 2K/Ni–MeAl became clear and sharp. In the presence of potassium, K<sup>+</sup> ions could interact not only with Al<sub>2</sub>O<sub>3</sub> to form K<sub>2</sub>Al<sub>2</sub>O<sub>4</sub> or KAlO<sub>2</sub> (JCPDS 450-850) (Figure S5) [46–48] but also with NiAl<sub>2</sub>O<sub>4</sub> through the cooperation of K<sup>+</sup> ions with tetrahedrally coordinated Al<sup>3+</sup> ions placed on the NiAl<sub>2</sub>O<sub>4</sub> surface [47,49]. This diminishes the interaction between Ni and Al<sub>2</sub>O<sub>3</sub>, causing of the growth in Ni particle size (Figure 2 and Table 1). The deconvolution results of the overlapped peaks in XRD patterns in the range of  $2\theta = 41^\circ$ – $50^\circ$  indicated that

the XRD peaks for metallic Ni were sharper in the xK/Ni–MeAl catalysts (Figure 5Ba–c) and broader in the xK/Ni–MaAl catalysts (Figure 5Bd–f). The Ni particle sizes in the xK/Ni–MaAl catalysts (Table 1), as calculated by the Scherrer equation, were much smaller than those in the xK/Ni–MeAl catalysts, indicating the prohibition of growth rate of Ni metallic crystal in the xK/Ni–MaAl catalyst.

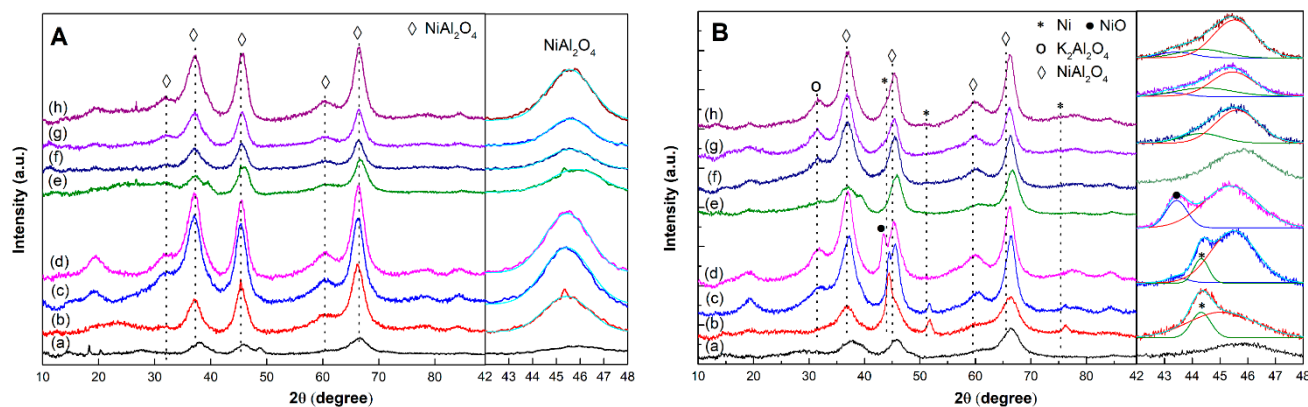


**Figure 5.** The XRD patterns of (A) calcined and (B) reduced catalysts: (a) MeAl, (b) Ni–MeAl, (c) 0.5K/Ni–MeAl, (d) 2K/Ni–MeAl, (e) MaAl, (f) Ni–MaAl, (g) 0.5K/Ni–MaAl, and (h) 2K/Ni–MaAl.

Figure 6 shows the details of the XPS spectra of Ni 2p, O1s, and Al 2p representing the electronic states of Ni, O, and Al on the reduced catalysts. In Figure 6A, three main deconvoluted peaks of Ni 2p data are observed, centered at 852.1, 854.9, and 856.9 eV. These peaks were ascribed to metallic Ni (Ni<sup>0</sup>), nickel oxide (Ni–O), and nickel aluminate (Ni–O–Al), respectively [50–54]. The K addition reduced a portion of the surface NiAl<sub>2</sub>O<sub>4</sub> and conversely increased the level of NiO, confirming the K–NiAl<sub>2</sub>O<sub>4</sub> interaction which was consistent with the XRD results. In Figure 6B, the O 1s spectra reveals a broad peak containing three main deconvoluted components: a peak at 530.5 eV attributed to lattice oxygen in Al<sub>2</sub>O<sub>3</sub>, a peak at 532.5 eV characterized for oxygen in O–H of aluminum oxo hydrides, and a peak at 533.5 eV assigned to oxygen in adsorbed water on the surface of Al<sub>2</sub>O<sub>3</sub> [55–57]. The water adsorbability of catalysts is strongly related to the acidity of  $\gamma$ -Al<sub>2</sub>O<sub>3</sub>, particularly for Lewis acidic sites. Oxygen in H<sub>2</sub>O has a lone electron pair that can share electrons with an Al<sup>3+</sup> acceptor in Al<sub>2</sub>O<sub>3</sub> (particularly Al<sup>3+</sup> in the tetrahedral interstice) to generate a covalent bond between Al in Al<sub>2</sub>O<sub>3</sub> and O in water. For the xK/Ni–MaAl catalysts, the adsorbed water peak intensity is higher in both Figure 6B,C than for xK/Ni–MeAl, and this peak intensity significantly decreased following the addition of higher K contents indicating increased AlO<sub>4</sub> in MaAl and the disappearance of Lewis acidic sites on the catalysts caused by K, which, in turn, was caused by the interaction between K<sup>+</sup> and Al<sup>3+</sup> in the tetrahedral interstice of Al<sub>2</sub>O<sub>3</sub>.

Scheme 1 summarizes the systematic changes in the compositions and structures of the prepared catalysts. The  $\gamma$ -Al<sub>2</sub>O<sub>3</sub> phase was found in the XRD pattern of both the MaAl and MeAl supports. The structure of Al<sub>2</sub>O<sub>3</sub> is traditionally described as a cubic defect spinel with a non-spinel fraction where the Al<sup>3+</sup> cations occupy both the octahedral (AlO<sub>6</sub>) and tetrahedral (AlO<sub>4</sub>) sites [58,59]. However, the AlO<sub>4</sub> site part was higher in the MaAl support. After the first impregnation step, Ni was introduced onto the surface of Al<sub>2</sub>O<sub>3</sub> (blue in Scheme 1) and formed multilayered structures on the alumina [38]. The introduced Ni precursor formed the surface NiAl<sub>2</sub>O<sub>4</sub>-like spinel phase (green in Scheme 1), which was a result of the interaction between NiO<sub>6</sub> and AlO<sub>4</sub> sites. NiAl<sub>2</sub>O<sub>4</sub> had a partially inverse spinel structure, where the bulk of Ni<sup>2+</sup> and Al<sup>3+</sup> cations occupied the octahedral and tetrahedral sites, respectively, and part of the Ni<sup>2+</sup> and Al<sup>3+</sup> cations inversely occupied the tetrahedral and octahedral sites [60,61]. An excess of Ni precursor existed in NiO (rock salt structure or amorphous structure) on the top of the NiAl<sub>2</sub>O<sub>4</sub> layer or on the top of Al<sub>2</sub>O<sub>3</sub> [62]. NiO on the Al<sub>2</sub>O<sub>3</sub> surface might indicate a weak Ni–AlO<sub>6</sub> interaction.

During the Ni addition process, the better access of  $\text{Ni}(\text{NO}_3)_2$  through macro/mesoporous channels onto MaAl that had higher portion of  $\text{AlO}_4$  sites, as evidenced by the XRD results, induced the preferential formation of  $\text{NiAl}_2\text{O}_4$  (not NiO) on the  $\text{Al}_2\text{O}_3$  surface over MaAl. As a result of the strong interaction between excessive NiO and  $\text{NiAl}_2\text{O}_4$ , NiO on this spinel layer was highly dispersed on the surface of MaAl. Owing to the difference in lattice structures,  $\text{NiAl}_2\text{O}_4$  and NiO exhibited different Ni reducibility values. Octahedral  $\text{Ni}^{2+}$  cations were reported as having higher reducibility than tetrahedral  $\text{Ni}^{2+}$  cations [38,63]. Therefore, in the TPR profiles (Figure 4), the peaks of NiO reduction appeared at a lower temperature compared with the peaks of Ni reduction in  $\text{NiAl}_2\text{O}_4$ . Likewise, the reduction peak of NiO–MaAl appeared at a lower temperature than that of NiO–MeAl, since NiO over MaAl was highly dispersed (Figure 4a,d). After reduction, Ni–MaAl contained highly dispersed Ni metallic particles and a  $\text{NiAl}_2\text{O}_4$  phase, whereas agglomerated Ni metallic and  $\text{NiAl}_2\text{O}_4$  phases were formed over the Ni–MeAl catalyst, which was evidenced by the XRD results. Following the second step, K was impregnated on the surface of Ni/ $\text{Al}_2\text{O}_3$  samples. K existed in  $\text{KAlO}_2$  with two different states: free  $\text{KAlO}_2$  phase (brown triangle, appearing only on the MeAl surface) and a highly dispersed phase on the alumina surface (brown rectangle), which was the result of K– $\text{Al}_2\text{O}_3$  and K– $\text{NiAl}_2\text{O}_4$  interactions, respectively. At a high temperature, K was able to interact with tetrahedral Al to form potassium aluminate ( $\text{KAlO}_2$ ) [64,65]. The typical structure of potassium aluminate is composed of corner-shared tetrahedral  $\text{AlO}_4$ , which causes sizable voids to be occupied by large K cations [65,66]. This interaction between K and tetrahedral Al could reduce the interaction between Ni and  $\text{Al}_2\text{O}_3$  [67]. As a result, the formation of the  $\text{NiAl}_2\text{O}_4$  phase was decreased, and the formation of the NiO phase was enhanced. Finally, the catalysts were partially reduced under the hydrogen environment to transform NiO into metallic Ni [68,69]. The strong K–Ni– $\text{Al}_2\text{O}_3$  interactions over xK/Ni–MaAl with the macro-porous channels inhibited the growth of Ni particles by K addition, maintaining the high dispersion of Ni on the catalyst surface. However, the different multiple interactions between K–Ni– $\text{Al}_2\text{O}_3$  over 2K/Ni–MeAl resulted in the formation of a triangular structure of  $\text{KAlO}_2$  and aggregation of NiO particles even after the reduction step.

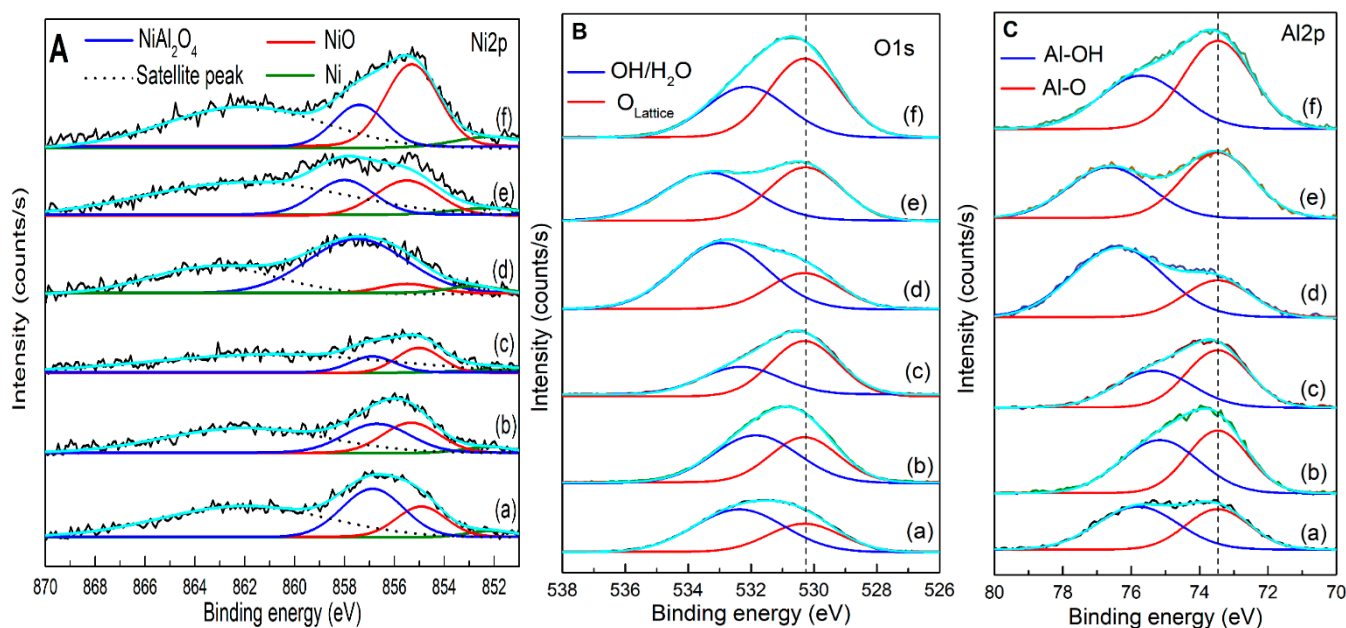
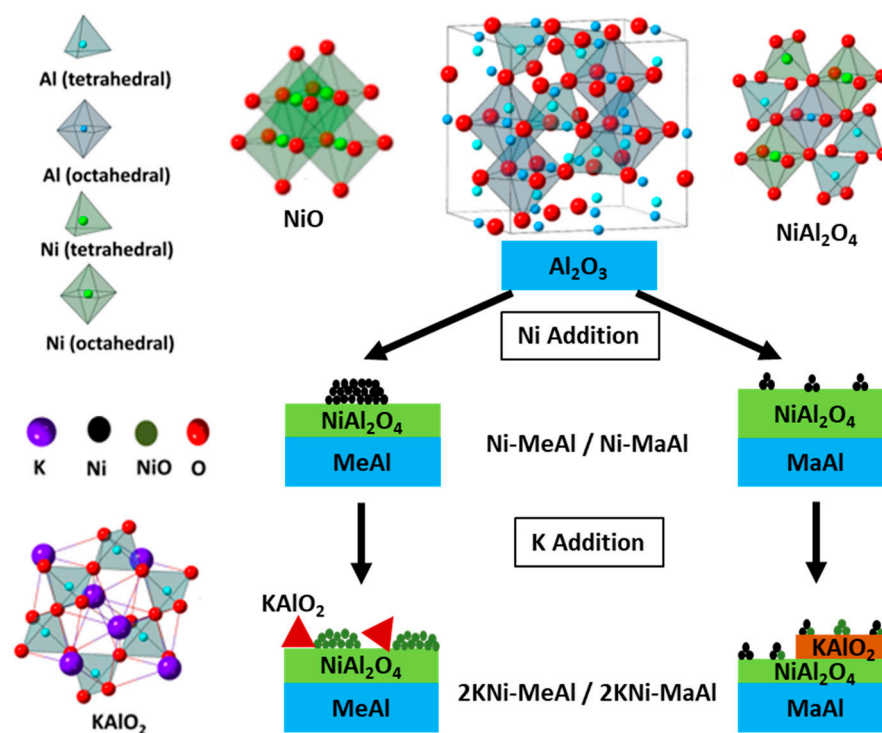


**Figure 6.** The XPS results of (A) Ni 2p, (B) O 1s, and (C) Al 2p: (a) Ni–MeAl, (b) 0.5K/Ni–MeAl, (c) 2K/Ni–MeAl, (d) Ni–MaAl, (e) 0.5K/Ni–MaAl, and (f) 2K/Ni–MaAl.



**Scheme 1.** Illustration of Ni–alumina and K–alumina/nickel aluminate interactions during the preparation steps.

## 2.2. Catalytic Activity

Steam reforming of 1-MN over the xK/Ni–MeAl and xK/Ni–MaAl catalysts was conducted at 600 °C for 2 h. The reaction results of the xK/Ni–Al catalysts are listed in Table 2. Without a catalyst (blank test), a low percentage of 1-MN (6.2%) was converted by thermal cracking, where 1-MN could be cracked through the expansion of C–C bonds, followed by the formation of hydrocarbon radicals [70], which could react together to form a heavier hydrocarbon, particularly coke. In the gas products, the majority of thermal cracking was linked to CH<sub>4</sub> and C<sub>2</sub>+ (C<sub>2</sub> gases) as the weak C–C bond between the methyl group and aromatic ring in 1-MN was easily broken into CH<sub>4</sub>. Over alumina supports only, a cracking reaction (C<sub>3</sub> and C<sub>4</sub> in gas products) might occur, raising the 1-MN conversions. In the presence of Ni containing catalysts, two more primary reactions (steam cracking and steam reforming) occurred over the Ni–MaAl and Ni–MeAl catalysts, resulting in higher 1-MN conversion (from 11.5 to 16.1 for Ni–MeAl and from 13.9 to 20.1 for Ni–MaAl) and a variation in liquid and gas selectivities for the different catalysts. For the xK/Ni–MaAl catalysts, the 1-MN conversions and C selectivities in gas were higher than those of the xK/Ni–MeAl catalysts. Moreover, for the xK/Ni–MaAl catalysts, ring-opening hydrocarbons and naphthalene (groups (1) and (3)) were the main components of liquid products, whereas for the xK/Ni–MeAl catalysts, there was a decrease in the proportion of these compounds and an increase in the heavier hydrocarbons (Anthracene—group (4)). Figure 7 shows the effect of K addition on 1-MN conversion. The 1-MN conversions after 2 h reaction linearly dropped for the xK/Ni–MeAl catalysts with increasing x values (x = 0: 16.1%; x = 0.5: 11.3%; and x = 2: 6.9%) while slightly changing into a volcano pattern for the xK/Ni–MaAl catalysts (x = 0: 20.1%; x = 0.5: 23.1%; and x = 2: 20.4%). This confirmed that a small K dopant content on Ni–MaAl supports could enhance the catalytic performance because of the macro/mesoporous channels and K–Ni–Al<sub>2</sub>O<sub>3</sub> interactions in MaAl catalyst. There was no effect of K on the performance of MeAl catalysts.

**Table 2.** Conversions and product distributions of 1-MN steam reforming over different catalysts (reaction conditions: T = 600 °C, t = 2 h, mass of catalyst = 0.25 g, loading rate of 1-MN = 0.1 mL/min, and water pump rate = 0.4 mL/min).

Catalysts	Conversion (%)	C-Selectivity in Products (%)			Liquid Product Distribution (%)			
		Coke	Gas	Liquid	(1)	(2)	(3)	(4)
Blank test	6.2	3.3	26.1	70.6	0.1	0.6	45.7	53.6
MeAl	11.5	0.4	22.9	76.8	40.8	12.4	40.1	22.7
Ni-MeAl	16.1	0.3	49.8	49.9	0	13.2	86.5	0.2
0.5K/Ni-MeAl	11.3	0.6	48.9	50.5	1.1	2.2	91	5.7
2K/Ni-MeAl	6.9	0.7	55.2	44.1	10.4	1.3	63.2	25.2
MaAl	13.9	0.3	47.0	52.7	28.9	8.6	56.8	5.8
Ni-MaAl	20.1	0.5	56.9	42.5	1.4	0.9	91.9	5.8
0.5K/Ni-MaAl	23.1	0.5	65.4	34.1	11.0	1.3	80.4	7.2
2K/Ni-MaAl	20.4	0.4	55.1	44.4	30.6	0.6	63.4	5.4

(1) Heptane, (2) Toluene, (3) Naphthalene, and (4) Anthracene (Figure S7, see Supplementary Data).

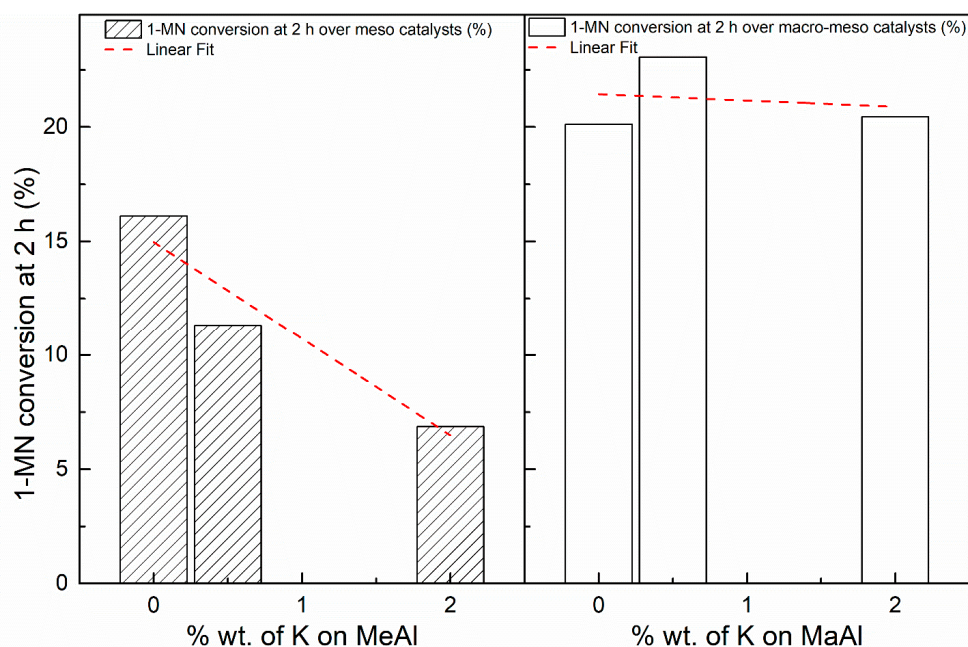


**Figure 7.** Dependence of 1-MN conversion on K percent on different supports (MeAl and MaAl).

In the xK/Ni-MaAl and xK/Ni-MeAl catalysts, Ni surfaces served as active sites for both steam reforming and steam cracking of 1-MN [71]. Steam reforming was competitive with steam cracking even though we reported that the reaction at 600 °C would prefer steam reforming over steam cracking in our previous study [52]. In steam reforming, 1-MN was oxidized into CO and H<sub>2</sub> gases by active oxygen species formed over Ni sites. In steam cracking, a hydrocarbon could potentially be oxidized by the OH group through the opening of the central aromatic ring, the release of CO<sub>2</sub> in the gas products, and ring-opening hydrocarbons. In Table 3, the higher CO<sub>2</sub> and lower CO portions in the gas composition of the Ni-MeAl catalyst indicate the relative dominance of steam cracking. In contrast, steam reforming occurred strongly over the xK/Ni-MaAl catalysts, generating more CO and less CO<sub>2</sub> in the gas composition (Table 3) and higher ring-opening hydrocarbon portions in the liquid product distributions (Table 2). For the xK/Ni-MaAl catalysts, it is possible that the additional nickel sites generated through K-NiAl<sub>2</sub>O<sub>4</sub> interactions to favor steam reforming, as evidenced by the lower portion of CH<sub>4</sub> and C<sub>2</sub>+ and the higher portion of CO and H<sub>2</sub> in the gas compositions (Table 3 and Figure S6, see Supplementary Data). As shown in the results, the TOF (H<sub>2</sub>) values were also higher for the xK/Ni-MaAl catalysts

(Table 3). Even with high K contents (2K/Ni–MaAl), a rise in the K–Ni interaction on the Ni surface or K coverage on Ni active sites led to a small decrease in steam reforming conversion (Table 2 and Figure 7), which also resulted in a small decrease in TOF ( $H_2$ ) value (Table 3). At the same time, the results for the xK/Ni–MeAl catalysts were almost the opposite compared with those for xK/Ni–MaAl catalysts. Most nickel active sites over the xK/Ni–MeAl catalysts disappeared readily because of the oligomerization of Ni particles by the added potassium, dramatically reducing both steam reforming and steam cracking. As shown in Table 3 and Figure S6 (see Supplementary Data), hydrogen and CO gases were almost entirely absent for 2K/Ni–MeAl. The high K coverage on Ni surfaces for 0.5K/Ni–MeAl and 2K/Ni–MeAl induced an increase in thermal cracking, which caused a rapid decrease in 1-MN conversion from 16.1% (Ni–MeAl) to 6.9% (2K/Ni–MeAl) (see Table 2) and the disappearance of  $H_2$  and CO while enhancing the  $C_2+$  portion in gas products (Table 3). Figure 8 represents a linear fit of the relationship between the steam reforming products ( $H_2 + CO$ ) and the Ni sites. There was a strong correlation between steam reforming and the Ni metallic sites ( $R^2 = 0.88$ ), indicating that the bigger Ni particles as a result of K addition reduced steam reforming.

**Table 3.** Gas compositions under the 1-h and 600 °C reaction conditions.

Catalysts	$H_2$	CO	$CO_2$	$CH_4$	$C_2+$	TOF ( $H_2$ ) (mol/mol.h)	$(H_2 + CO)/(CH_4 + C_2+)$ Mole Ratio
Blank test	0	0	0	66	34	-	0.0
MeAl	0	0	6	66	28	-	0.0
Ni–MeAl	28	29	38	3	2	736	11.4
0.5K/Ni–MeAl	18	8	12	48	15	430	0.4
2K/Ni–MeAl	0	0	22	38	40	-	0.0
MaAl	0	0	5	62	33	-	0.0
Ni–MaAl	28	26	9	20	17	577	1.5
0.5K/Ni–MaAl	43	26	7	14	10	952	2.9
2K/Ni–MaAl	41	26	9	16	7	950	2.9

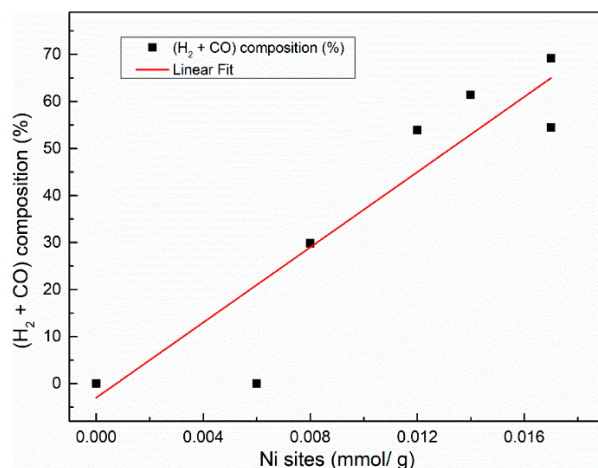
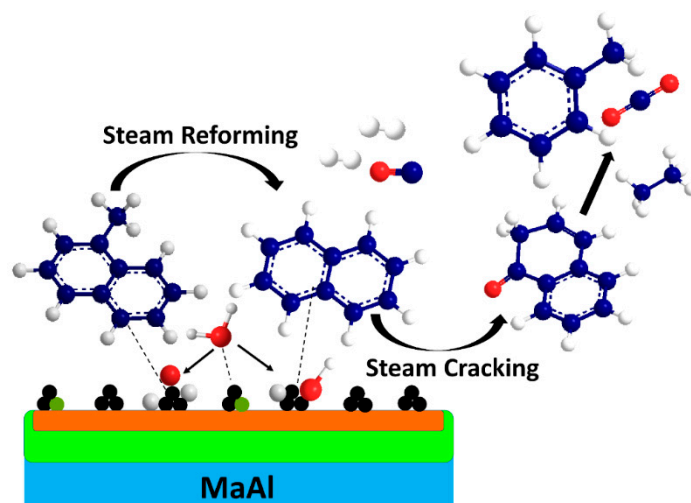


**Figure 8.** A linear fit of relationship between the steam reforming products ( $H_2 + CO$ ) and the Ni sites.

Scheme 2 shows the possible steam reforming reaction routes of the reaction of 1-MN with steam over the xK/Ni–Al catalysts. First, over the Ni sites on nickel-containing catalysts, adsorbed steam was dissociated into a hydroxyl group and hydrogen. This OH group was further dissociated into active H and O species that were adsorbed on the Ni surface [72,73]. The strong interaction between Ni and the supports or a high Ni dispersion decreased the energy barrier of O–H cleavage, thus promoting steam dissociation. Over the xK/Ni–MaAl catalysts, additional active O species were generated from steam decomposition as O–H cracking in the OH group appeared to be favorable which may have been caused by the high Ni dispersion on MaAl. Therefore, steam reforming occurred

predominantly over the xK/Ni–MaAl catalysts, resulting in higher carbon selectivity in the gas (Table 2) and generation of more CO and H<sub>2</sub> in the gas (Table 3). Through the oxidation of adsorbed 1-MN by O species from steam on Ni sites, the aromatic ring in 1-MN proved difficult to open directly to form lighter hydrocarbons. As a result, a majority of the liquid products were classified as group (3) (Figure S7, see Supplementary Data) for the xK/Ni–MaAl catalysts (Table 2).



**Scheme 2.** Main reaction pathways of steam reforming.

When the oxidation of 1-MN was successfully completed, the H<sub>2</sub>/CO + CO<sub>2</sub> ratio reached its highest value at 2.45, which was roughly estimated from the chemical equation (Reaction 4). However, among all Ni-containing catalysts, this ratio was the lowest for Ni–MeAl (0.42) and highest for 0.5K/Ni–MaAl (1.26) (Table 3). This demonstrated that 1-MN was oxidized systematically over Ni sites, and the high percentage of aromatic products (2) in liquids contributed to the difficulty of oxidation of a large molecule such as 1-methyl naphthalene over xK/Ni–Al catalysts. The time on stream of 1-MN conversion for all catalysts is shown in Figure S8 (see Supplementary Data). Conversion of 1-MN for the xK/Ni–MeAl catalysts (dashed lines) were lower than those for xK/Ni–MaAl catalysts (solid lines). In the time on stream of (H<sub>2</sub> + CO) composition in the gas products (Figure S6, see Supplementary Data), the steam reforming products (H<sub>2</sub> and CO) were produced more over xK/Ni–MaAl catalysts (solid lines) compared to the xK/Ni–MeAl catalysts (dashed lines), which reflected the better catalytic performance of xK/Ni–MaAl catalysts in steam reforming of 1-MN.

### 3. Materials and Methods

#### 3.1. Catalyst Preparation

Mesoporous alumina-supported nickel and potassium (xK/Ni–MeAl) and macroporous alumina-supported nickel and potassium (xK/Ni–MaAl) (x = 0%, 0.5%, and 2%) catalysts were synthesized using the incipient wetness impregnation method to impregnate a KNO<sub>3</sub> salt solution to reach x wt.% K on Ni–MeAl and Ni–MaAl catalysts. All catalysts were calcined in air at 600 °C for 6 h. The Ni–MeAl, Ni–MaAl, yK/MeAl, and yK/MaAl (y = 2% and 5%) catalysts were prepared using the same method used for xK/Ni–MeAl and xK/Ni–MaAl catalysts. However, the impregnation of a Ni(NO<sub>3</sub>)<sub>2</sub> salt solution was predicted to reach 10 wt.% Ni on MeAl and MaAl supports.

The preparation of MaAl has previously been described in detail [74]. The ethanol-to-water ratio in the washing step was 1:3, and the calcination temperature was 600 °C. The MeAl was prepared using the same method used for MaAl: a triblock copolymer Pluronic P123 (PEG–PPG–PEG) was used to create a porous structure rather than polystyrene beads as a macroporous structure template.

### 3.2. Characterization

The Brunauer–Emmett–Teller (BET) surface area and pore-size distribution of the prepared catalysts were determined by implementing the nitrogen adsorption/desorption method on a Micromeritics ASAP 2020 apparatus (Norcross, GA, USA). The catalysts were pretreated at 300 °C for 6 h prior to measurement. Ammonia temperature-programmed desorption (NH<sub>3</sub>-TPD), hydrogen temperature-programmed desorption (H<sub>2</sub>-TPD), and hydrogen temperature-programmed reduction (H<sub>2</sub>-TPR) were carried out in a multipurpose analytical system (BELCAT-M, MicrotracBEL Corp., Osaka, Japan) using a thermal conductivity detector (TCD). For NH<sub>3</sub>-TPD, catalysts were pretreated at 600 °C for 2 h in a carrier gas (in this case, helium gas). Once the ammonia gas (5% in helium) had been adsorbed at 50 °C for 1 h, the temperature was increased to 600 °C (ramping rate = 2 °C/min under carrier gas), and the desorbed ammonia was recorded using the TCD sensor. A similar procedure was applied in the H<sub>2</sub>-TPD experiment, where the adsorbed gas was hydrogen (5% H<sub>2</sub> in N<sub>2</sub>) and the carrier gas was N<sub>2</sub>. For the H<sub>2</sub>-TPR experiment, the catalysts were oxidized by oxygen (5% in helium) at 600 °C for 2 h prior to the start of the reduction step. The oxidized catalysts were reduced by hydrogen, and the temperature was elevated from 50 °C to 900 °C (ramping rate = 2 °C/min).

X-ray diffraction (XRD) data were obtained using a Rigaku RAD-3C diffractometer (Rigaku Corp., Tokyo, Japan) with Cu K $\alpha$  radiation ( $\lambda = 1.5418 \text{ \AA}$ ) at a scan rate of 2°(2 $\theta$ )/min, operated at 35 kV and 20 mA. On the basis of the XRD patterns, Ni crystal sizes were calculated using the Scherrer Equation (1).

$$\text{Crystalline size (L)} = \frac{K\lambda}{B\cos(\theta)} \quad (1)$$

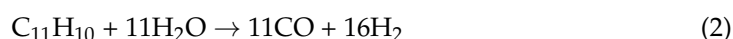
X-ray photoelectron spectroscopy (XPS) data were obtained using Thermo K-Alpha XPS with an Al-K $\alpha$  X-ray source (Thermo Fisher Scientific, Waltham, MA, USA). The XPS results were collected using an X-ray spot size of 400  $\mu\text{m}$ , pass energy of 80 eV, and an energy step size of 0.1 eV.

The surface morphology of the catalysts was characterized using a field-emission scanning electron microscope (SEM; JEOL JSM-600F, Tokyo, Japan) and a high-resolution transmission electron microscopy instrument (TEM; JEM-2100F, JEOL, Tokyo, Japan). Specimens were prepared by suspending and grinding in an ethanol solution, and two drops of ethanol solution containing the ground catalyst powder were placed onto a carbon film-coated copper grid.

### 3.3. Reaction Test

Firstly, 0.25 g of catalyst power, placed in the middle of a quartz tube reactor (inner diameter of 9.1 mm), was reduced in situ in flowing hydrogen (12.8 mL/min) and helium (8.2 mL/min) at 600 °C for 2 h in a fix-bed reactor. After the reduction step, all hydrogen gas was removed by helium flow (8.2 mL/min). Secondly, the mixture of water flow (0.4 mL/min) was heated to 200 °C to vaporize water prior to entering the reactor. Subsequently, a flow of 1-MN was fed at 0.12 mL/min into the reactor. The catalyst performance test was carried out at 600 °C for 2 h, the steam to carbon ratio (S/C) was 2.43 and the weight hourly space velocity (WHSV) was 125 h<sup>-1</sup>.

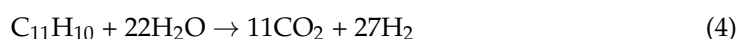
Steam reforming:



Water gas shift:



Combination of steam reforming and water gas shift:



For product analysis, light gases ( $H_2$ , CO,  $CO_2$ , and  $CH_4$ ) and  $C_2$ – $C_4$  gases were analyzed using a gas chromatography–TCD (Acme 6100 GC, YL Instrument Co., Ltd., Dongan-gu, Anyang, Republic of Korea) with Carboxen 1000 and an HP-PLOT Q column, respectively. The liquid products were evaluated by gas chromatography with a flame-ionization detection machine (Agilent 6890 N Network GC, Agilent Technologies, Inc., Santa Clara, CA, USA) using an HP-5 column. The coke amount was determined by thermogravimetric analysis (TG Q50, TA instrument, New Castle, DE, USA).

The carbon selectivities of the liquid ( $S_{C-Liquid}$ , mol%), gas ( $S_{C-Gas}$ , mol%), and coke ( $S_{C-Coke}$ , mol%) were defined as the moles of carbon in the liquid, gas, and coke products, respectively, divided by the moles of carbon in the reacted 1-MN (as a percentage). Conversion (C, mol%) was defined as the moles of carbon in the reacted 1-MN divided by the moles of carbon of the total 1-MN loaded into the reactor during reaction time. The reaction rate, gas composition, and turnover frequency (TOF) were calculated using the equations below:

$$\text{Carbon selectivity of gas (mol, \%)} = \frac{\text{Mole of carbon in gas}}{\text{Mole of carbon in reacted 1-MN}} \times 100 \quad (5)$$

$$\text{Carbon selectivity of liquid (mol, \%)} = \frac{\text{Mole of carbon in liquid}}{\text{Mole of carbon in reacted 1-MN}} \times 100 \quad (6)$$

$$\text{Carbon selectivity of coke (mol, \%)} = \frac{\text{Mole of carbon in coke}}{\text{Mole of carbon in reacted 1-MN}} \times 100 \quad (7)$$

$$\text{Conversion (mol, \%)} = \frac{\text{Mole of carbon in reacted 1-MN}}{\text{Mole of carbon in fed 1-MN}} \times 100 \quad (8)$$

$$\text{Gas composition (mol, \%)} = \frac{\text{Mole of each gas product}}{\text{Total mole of gas products}} \times 100 \quad (9)$$

$$\text{TOF for } H_2 = \frac{\text{Mole of } H_2 \text{ gas produced}}{\text{Mole of Ni sites} \times \text{reaction time}} \quad (10)$$

#### 4. Conclusions

Hierarchical MaAl and MeAl were used as supports for xK/Ni– $Al_2O_3$  catalysts in the steam reforming of 1-methyl naphthalene at a low temperature (600 °C) in a fixed-bed reactor. By adding different potassium content percentages (0%, 0.5%, and 2%) on nickel-containing supports, the effect of a hierarchically ordered macroporous structure on the interactions between K or Ni–support and K–Ni $Al_2O_4$ , alongside steam reforming performance, was observed in this study. We found that Ni nanoparticles were highly dispersed on the catalyst surface of MaAl due to the K–Ni– $Al_2O_3$  interaction whereas the metallic Ni was agglomerated over MeAl. The increased size of Ni metallic particles suppressed hydrogen adsorption on the nickel sites during the reaction, reducing steam reforming. Therefore, the multiple interactions between K–Ni– $Al_2O_3$  over MaAl created more nanosized Ni particles, thereby enhancing steam reforming, leading to high 1-MN conversion, improved carbon selectivity of gas and high hydrogen and CO portions in the gas phase.

**Supplementary Materials:** The following supporting information can be downloaded at: <https://www.mdpi.com/article/10.3390/catal12121542/s1>, Figure S1: The SEM images of (A) Ni–MaAl and (B) 2K/Ni–MaAl. Figure S2: The TEM and TEM-EDS images of Ni–MaAl. Figure S3: The TEM and TEM-EDS images of 0.5K/Ni–MeAl. Figure S4: The TEM and TEM-EDS images of 2K/Ni–MeAl. Figure S5: XRD patterns of (a) MeAl, (b) 2K/MeAl, (c) 5K/MeAl, (d) MaAl, (e) 2K/MaAl, and (f) 5K/MaAl. Figure S6: Time on the stream of total  $H_2$  and CO composition in gas products. The values of the ( $H_2 + CO$ ) composition from Blank test and the reactions over MeAl, 2K/Ni–MeAl, MaAl are zero and not clearly shown in the graph. Figure S7: A typical gas chromatogram of liquid products (reaction conditions: Ni–MeAl catalyst, T = 600 oC, t = 2 h, mass of catalyst = 0.25g,

F1-methylnaphthalene = 0.14 ml/min): (1) ring-Opened products, (2) aromatics, and (3) condensed products or polymerizates. Figure S8: Time on the stream of 1-MN conversions for all catalysts.

**Author Contributions:** L.T.D. performed the experiments and wrote a draft of the paper; H.N.-P. performed the experiments and contributed to data analysis; N.N.P. contributed to data collections; D.H.J. contributed to editing the paper; E.W.S. supervised the work and polished the paper. All authors have read and agreed to the published version of the manuscript.

**Funding:** This work was supported by the National Research Foundation of Korea (NRF) grant funded by the Korea government (MSIT) (No. 2020R1A4A4079954 and 2021R1A2B5B01001448) and “Regional Innovation Strategy (RIS) program” through the NRF funded by the Ministry of Education (MOE) (No. 2021RIS-003-1345341781).

**Data Availability Statement:** The data presented in this study are available on request from the corresponding author.

**Conflicts of Interest:** The authors declare no conflict of interest.

## References

1. US Energy Information Administration, Monthly Energy Review. April 2018. Available online: <https://www.eia.gov/totalenergy/data/annual/> (accessed on 13 November 2018).
2. Guizani, C.; Valin, S.; Billaud, J.; Peyrot, M.; Salvador, S. Biomass fast pyrolysis in a drop tube reactor for bio oil production: Experiments and modeling. *Fuel* **2017**, *207*, 71–84. [CrossRef]
3. Gómez, N.; Banks, S.; Nowakowski, D.; Rosas, J.; Cara, J.; Sánchez, M.; Bridgwater, A. Effect of temperature on product performance of a high ash biomass during fast pyrolysis and its bio-oil storage evaluation. *Fuel Process. Technol.* **2018**, *172*, 97–105. [CrossRef]
4. Serrano-Ruiz, J.C. Biomass conversion technologies: Catalytic conversion technologies. In *Biorefineries*; Springer: Berlin/Heidelberg, Germany, 2017; pp. 113–121.
5. Bridgwater, A. Biomass conversion technologies: Fast pyrolysis liquids from biomass: Quality and upgrading. In *Biorefineries*; Springer: Berlin/Heidelberg, Germany, 2017; pp. 55–98.
6. Wheeldon, I.; Christopher, P.; Blanch, H. Integration of heterogeneous and biochemical catalysis for production of fuels and chemicals from biomass. *Curr. Opin. Biotechnol.* **2017**, *45*, 127–135. [CrossRef] [PubMed]
7. Gouveia, L.; Passarinho, P.C. Biomass conversion technologies: Biological/biochemical conversion of biomass. In *Biorefineries*; Springer: Berlin/Heidelberg, Germany, 2017; pp. 99–111.
8. Dhepe, P.; Tomishige, K.; Wu, K.C.W. Catalytic conversion of biomass. *ChemCatChem* **2017**, *9*, 2613–2614. [CrossRef]
9. Sansaniwal, S.; Pal, K.; Rosen, M.; Tyagi, S. Recent advances in the development of biomass gasification technology: A comprehensive review. *Renew. Sustain. Energy Rev.* **2017**, *72*, 363–384. [CrossRef]
10. Wang, L.; Li, D.; Koike, M.; Koso, S.; Nakagawa, Y.; Xu, Y.; Tomishige, K. Catalytic performance and characterization of Ni-Fe catalysts for the steam reforming of tar from biomass pyrolysis to synthesis gas. *Appl. Catal. A Gen.* **2011**, *392*, 248–255. [CrossRef]
11. Zhang, R.; Wang, Y.; Brown, R.C. Steam reforming of tar compounds over Ni/olivine catalysts doped with CeO<sub>2</sub>. *Energy Convers. Manag.* **2007**, *48*, 68–77. [CrossRef]
12. Furusawa, T.; Tsutsumi, A. Comparison of Co/MgO and Ni/MgO catalysts for the steam reforming of naphthalene as a model compound of tar derived from biomass gasification. *Appl. Catal. A Gen.* **2005**, *278*, 207–212. [CrossRef]
13. Li, D.; Tamura, M.; Nakagawa, Y.; Tomishige, K. Metal catalysts for steam reforming of tar derived from the gasification of lignocellulosic biomass. *Bioresour. Technol.* **2015**, *178*, 53–64. [CrossRef]
14. Kechagiopoulos, P.; Angeli, S.; Lemonidou, A. Low temperature steam reforming of methane: A combined isotopic and microkinetic study. *Appl. Catal. B Environ.* **2017**, *205*, 238–253. [CrossRef]
15. Jiao, Y.; Zhang, J.; Du, Y.; Sun, D.; Wang, J.; Chen, Y.; Lu, J. Steam reforming of hydrocarbon fuels over M (Fe, Co, Ni, Cu, Zn)–Ce bimetal catalysts supported on Al<sub>2</sub>O<sub>3</sub>. *Int. J. Hydrogen Energy* **2016**, *41*, 10473–10482. [CrossRef]
16. Artetxe, M.; Nahil, M.A.; Olazar, M.; Williams, P.T. Steam reforming of phenol as biomass tar model compound over Ni/Al<sub>2</sub>O<sub>3</sub> catalyst. *Fuel* **2016**, *184*, 629–636. [CrossRef]
17. Artetxe, M.; Alvarez, J.; Nahil, M.A.; Olazar, M.; Williams, P.T. Steam reforming of different biomass tar model compounds over Ni/Al<sub>2</sub>O<sub>3</sub> catalysts. *Energy Convers. Manag.* **2017**, *136*, 119–126. [CrossRef]
18. Salehi, E.; Azad, F.S.; Harding, T.; Abedi, J. Production of hydrogen by steam reforming of bio-oil over Ni/Al<sub>2</sub>O<sub>3</sub> catalysts: Effect of addition of promoter and preparation procedure. *Fuel Process. Technol.* **2011**, *92*, 2203–2210. [CrossRef]
19. Marino, F.; Boveri, M.; Baronetti, G.; Laborde, M. Hydrogen production from steam reforming of bioethanol using Cu/Ni/K/γ-Al<sub>2</sub>O<sub>3</sub> catalysts. Effect of Ni. *Int. J. Hydrogen Energy* **2001**, *26*, 665–668. [CrossRef]
20. Li, M.-R.; Lu, Z.; Wang, G.-C. The effect of potassium on steam-methane reforming on the Ni<sub>4</sub>/Al<sub>2</sub>O<sub>3</sub> surface: A DFT study. *Catal. Sci. Technol.* **2017**, *7*, 3613–3625. [CrossRef]
21. Borowiecki, T.; Denis, A.; Rawski, M.; Gołbiowski, A.; Stołecki, K.; Dmytryk, J.; Kotarba, A. Studies of potassium-promoted nickel catalysts for methane steam reforming: Effect of surface potassium location. *Appl. Surf. Sci.* **2014**, *300*, 191–200. [CrossRef]

22. Wu, G.; Zhang, C.; Li, S.; Han, Z.; Wang, T.; Ma, X.; Gong, J. Hydrogen production via glycerol steam reforming over Ni/Al<sub>2</sub>O<sub>3</sub>: Influence of nickel precursors. *ACS Sustain. Chem. Eng.* **2013**, *1*, 1052–1062. [[CrossRef](#)]
23. Sehested, J. Sintering of nickel steam-reforming catalysts. *J. Catal.* **2003**, *217*, 417–426. [[CrossRef](#)]
24. Xavier, K.; Sreekala, R.; Rashid, K.; Yusuff, K.; Sen, B. Doping effects of cerium oxide on Ni/Al<sub>2</sub>O<sub>3</sub> catalysts for methanation. *Catal. Today* **1999**, *49*, 17–21. [[CrossRef](#)]
25. Li, J.; Zhou, L.; Zhu, Q.; Li, H. CO methanation over a macro-mesoporous Al<sub>2</sub>O<sub>3</sub> supported Ni catalyst in a fluidized bed reactor. *RSC Adv.* **2015**, *5*, 64486–64494. [[CrossRef](#)]
26. Yu, N.; Rahman, M.M.; Chen, J.; Sun, J.; Engelhard, M.; Hernandez, X.I.P.; Wang, Y. Steam reforming of simulated bio-oil on K-Ni-Cu-Mg-Ce-O/Al<sub>2</sub>O<sub>3</sub>: The effect of K. *Catal. Today* **2019**, *323*, 183–190. [[CrossRef](#)]
27. Alstrup, I.; Clausen, B.; Olsen, C.; Smits, R.; Rostrup-Nielsen, J. Promotion of steam reforming catalysts. In *Studies in Surface Science and Catalysis*; Elsevier: Amsterdam, The Netherlands, 1998; Volume 119, pp. 5–14.
28. Sehested, J.; Gelten, J.A.; Helveg, S. Sintering of nickel catalysts: Effects of time, atmosphere, temperature, nickel-carrier interactions, and dopants. *Appl. Catal. A Gen.* **2006**, *309*, 237–246. [[CrossRef](#)]
29. Xu, J.; Liu, J.; Zhao, Z.; Xu, C.; Zheng, J.; Duan, A.; Jiang, G. Easy synthesis of three-dimensionally ordered macroporous La<sub>1-x</sub>K<sub>x</sub>CoO<sub>3</sub> catalysts and their high activities for the catalytic combustion of soot. *J. Catal.* **2011**, *282*, 1–12. [[CrossRef](#)]
30. Park, N.-K.; Seong, Y.B.; Kim, M.J.; Kim, Y.S.; Lee, T.J. Synthesis of meso- and macro-porous aluminosilicate over micro-channel plate as support material for production of hydrogen by water-gas shift (WGS). *Int. J. Precis. Eng. Manuf.* **2015**, *16*, 1239–1244. [[CrossRef](#)]
31. Du, J.; Lai, X.; Yang, N.; Zhai, J.; Kisailus, D.; Su, F.; Wang, D.; Jiang, L. Hierarchically ordered macro-mesoporous TiO<sub>2</sub>-graphene composite films: Improved mass transfer, reduced charge recombination, and their enhanced photocatalytic activities. *ACS Nano* **2011**, *5*, 590–596. [[CrossRef](#)]
32. Semeykina, V.S.; Parkhomchuk, E.V.; Polukhin, A.V.; Parunin, P.D.; Lysikov, A.I.; Ayupov, A.B.; Cherepanova, S.V.; Kanazhevskiy, V.V.; Kaichev, V.V.; Glazneva, T.S. CoMoNi catalyst texture and surface properties in heavy oil processing. Part I: Hierarchical macro/mesoporous alumina support. *Ind. Eng. Chem. Res.* **2016**, *55*, 3535–3545. [[CrossRef](#)]
33. Do, L.T.; Nguyen-Huy, C.; Shin, E.W. NiK/yCe<sub>x</sub>Zr<sub>1-x</sub>O<sub>2</sub>-macroporous Al<sub>2</sub>O<sub>3</sub> catalysts for cracking of vacuum residual oil with steam. *Appl. Catal. A Gen.* **2016**, *525*, 23–30. [[CrossRef](#)]
34. Rahmani, S.; Rezaei, M.; Meshkani, F. Preparation of highly active nickel catalysts supported on mesoporous nanocrystalline γ-Al<sub>2</sub>O<sub>3</sub> for CO<sub>2</sub> methanation. *J. Ind. Eng. Chem.* **2014**, *20*, 1346–1352. [[CrossRef](#)]
35. Shang, Z.; Li, S.; Li, L.; Liu, G.; Liang, X. Highly active and stable alumina supported nickel nanoparticle catalysts for dry reforming of methane. *Appl. Catal. B Environ.* **2017**, *201*, 302–309. [[CrossRef](#)]
36. Li, C.; Chen, Y.-W. Temperature-programmed-reduction studies of nickel oxide/alumina catalysts: Effects of the preparation method. *Thermochim. Acta* **1995**, *256*, 457–465. [[CrossRef](#)]
37. Benrabaa, R.; Barama, A.; Boukhlof, H.; Guerrero-Caballero, J.; Rubbens, A.; Bordes-Richard, E.; Löfberg, A.; Vannier, R.-N. Physico-chemical properties and syngas production via dry reforming of methane over NiAl<sub>2</sub>O<sub>4</sub> catalyst. *Int. J. Hydrogen Energy* **2017**, *42*, 12989–12996. [[CrossRef](#)]
38. Heracleous, E.; Lee, A.; Wilson, K.; Lemonidou, A. Investigation of Ni-based alumina-supported catalysts for the oxidative dehydrogenation of ethane to ethylene: Structural characterization and reactivity studies. *J. Catal.* **2005**, *231*, 159–171. [[CrossRef](#)]
39. Kathiraser, Y.; Thitsartarn, W.; Sutthiumporn, K.; Kawi, S. Inverse NiAl<sub>2</sub>O<sub>4</sub> on LaAlO<sub>3</sub>-Al<sub>2</sub>O<sub>3</sub>: Unique catalytic structure for stable CO<sub>2</sub> reforming of methane. *J. Phys. Chem. C* **2013**, *117*, 8120–8130. [[CrossRef](#)]
40. Li, G.; Hu, L.; Hill, J.M. Comparison of reducibility and stability of alumina-supported Ni catalysts prepared by impregnation and co-precipitation. *Appl. Catal. A Gen.* **2006**, *301*, 16–24. [[CrossRef](#)]
41. Nguyen-Phu, H.; Shin, E.W. Disordered structure of ZnAl<sub>2</sub>O<sub>4</sub> phase and the formation of a Zn NCO complex in ZnAl mixed oxide catalysts for glycerol carbonylation with urea. *J. Catal.* **2019**, *373*, 147–160. [[CrossRef](#)]
42. Fleisher, M.; Golender, L.; Shimanskaya, M. Electronic charge distribution and Lewis acidity of surface aluminium atoms in γ-Al<sub>2</sub>O<sub>3</sub>: A quantum-chemical model. *J. Chem. Soc. Faraday Trans.* **1991**, *87*, 745–748. [[CrossRef](#)]
43. Tachikawa, H.; Tsuchida, T. The electronic states and Lewis acidity of surface aluminum atoms in γ-Al<sub>2</sub>O<sub>3</sub> model cluster: An ab initio MO study. *J. Mol. Catal. A Chem.* **1995**, *96*, 277–282. [[CrossRef](#)]
44. Sun, M.; Nelson, A.E.; Adjaye, J. Examination of spinel and nonspinel structural models for γ-Al<sub>2</sub>O<sub>3</sub> by DFT and Rietveld refinement simulations. *J. Phys. Chem. B* **2006**, *110*, 2310–2317. [[CrossRef](#)]
45. Prins, R. Location of the Spinel Vacancies in γ-Al<sub>2</sub>O<sub>3</sub>. *Angew. Chem. Int. Ed.* **2019**, *58*, 15548–15552. [[CrossRef](#)]
46. Wei, Q.; Hu, J.; Zhang, H.; Wang, G.; Yang, X. Efficient Synthesis of Dimethyl Carbonate via Transesterification from Ethylene Carbonate with Methanol Using KAlO<sub>2</sub>/γ-Al<sub>2</sub>O<sub>3</sub> Heterogeneous Catalyst. *ChemistrySelect* **2020**, *5*, 7826–7834. [[CrossRef](#)]
47. de Kroon, A.P.; Schäfer, G.W.; Aldinger, F. Crystallography of potassium aluminate K<sub>2</sub>O·Al<sub>2</sub>O<sub>3</sub>. *J. Alloys Compd.* **2001**, *314*, 147–153. [[CrossRef](#)]
48. Ma, H.; Li, S.; Wang, B.; Wang, R.; Tian, S. Transesterification of rapeseed oil for synthesizing biodiesel by K/KOH/γ-Al<sub>2</sub>O<sub>3</sub> as heterogeneous base catalyst. *J. Am. Oil Chem. Soc.* **2008**, *85*, 263–270. [[CrossRef](#)]
49. de Miguel, S.R.; Scelza, O.A.; Castro, A.A.; Soria, J. Characterization of γ-alumina doped with Li and K by infrared studies of CO adsorption and <sup>27</sup>Al-NMR. *Top. Catal.* **1994**, *1*, 87–94. [[CrossRef](#)]

50. Do, L.T.; Nguyen-Huy, C.; Shin, E.W. Effect of a  $CeyNi_{1-y}O_{2-\delta}$  solid solution on the oxidative cracking of vacuum residue over NiK/CeO<sub>2</sub>. *React. Kinet. Mech. Catal.* **2017**, *122*, 983–993. [[CrossRef](#)]
51. Do, L.T.; Nguyen-Huy, C.; Shin, E.W. Different Metal Support Interactions over NiK/Mixed Oxide Catalysts and Their Effects on Catalytic Routes in Steam Catalytic Cracking of Vacuum Residue. *ChemistrySelect* **2018**, *3*, 1827–1835. [[CrossRef](#)]
52. Do, L.T.; Shin, E.W. Reinforcement of steam oxidative cracking of 1-methyl naphthalene by the synergistic combination of hydrogenation and oxidation over nickel-containing mixed oxide catalysts. *J. Catal.* **2019**, *371*, 245–254. [[CrossRef](#)]
53. Xu, X.; Fu, Q.; Guo, X.; Bao, X. A highly active “NiO-on-Au” surface architecture for CO oxidation. *ACS Catal.* **2013**, *3*, 1810–1818. [[CrossRef](#)]
54. Shen, J.; Hayes, R.E.; Wu, X.; Semagina, N. 100 Temperature reduction of wet methane combustion: Highly active Pd–Ni/Al<sub>2</sub>O<sub>3</sub> catalyst versus Pd/NiAl<sub>2</sub>O<sub>4</sub>. *ACS Catal.* **2015**, *5*, 2916–2920. [[CrossRef](#)]
55. Gupta, S.; Ramamurthy, P.C.; Madras, G. Synthesis and characterization of flexible epoxy nanocomposites reinforced with amine functionalized alumina nanoparticles: A potential encapsulant for organic devices. *Polym. Chem.* **2011**, *2*, 221–228. [[CrossRef](#)]
56. Ozensoy, E.; Szanyi, J.; Peden, C.H. Interaction of water with ordered  $\theta$ -Al<sub>2</sub>O<sub>3</sub> ultrathin films grown on NiAl (100). *J. Phys. Chem. B* **2005**, *109*, 3431–3436. [[CrossRef](#)] [[PubMed](#)]
57. Cárdenas-Arenas, A.; Quindimil, A.; Davó-Quiñonero, A.; Bailón-García, E.; Lozano-Castello, D.; De-La-Torre, U.; Pereda-Ayo, B.; González-Marcos, J.A.; González-Velasco, J.R.; Bueno-López, A. Isotopic and in situ DRIFTS study of the CO<sub>2</sub> methanation mechanism using Ni/CeO<sub>2</sub> and Ni/Al<sub>2</sub>O<sub>3</sub> catalysts. *Appl. Catal. B Environ.* **2020**, *265*, 118538. [[CrossRef](#)]
58. Smrčok, L.; Langer, V.; Křest'án, J.  $\gamma$ -Alumina: A single-crystal X-ray diffraction study. *Acta Crystallogr. Sect. C Cryst. Struct. Commun.* **2006**, *62*, i83–i84. [[CrossRef](#)]
59. Samain, L.; Jaworski, A.; Edén, M.; Ladd, D.M.; Seo, D.-K.; Garcia-Garcia, F.J.; Häussermann, U. Structural analysis of highly porous  $\gamma$ -Al<sub>2</sub>O<sub>3</sub>. *J. Solid State Chem.* **2014**, *217*, 1–8. [[CrossRef](#)]
60. Elias, I.; Soon, A.; Huang, J.; Haynes, B.S.; Montoya, A. Atomic order, electronic structure and thermodynamic stability of nickel aluminate. *Phys. Chem. Chem. Phys.* **2019**, *21*, 25952–25961. [[CrossRef](#)]
61. Roelofsen, J.N.; Peterson, R.C.; Raudsepp, M. Structural variation in nickel aluminate spinel (NiAl<sub>2</sub>O<sub>4</sub>). *Am. Mineral.* **1992**, *77*, 522–528.
62. Dubal, D.P.; Gomez-Romero, P.; Sankapal, B.R.; Holze, R. Nickel cobaltite as an emerging material for supercapacitors: An overview. *Nano Energy* **2015**, *11*, 377–399.
63. Kirumakki, S.R.; Shpeizer, B.G.; Sagar, G.V.; Chary, K.V.; Clearfield, A. Hydrogenation of naphthalene over NiO/SiO<sub>2</sub>–Al<sub>2</sub>O<sub>3</sub> catalysts: Structure–activity correlation. *J. Catal.* **2006**, *242*, 319–331. [[CrossRef](#)]
64. Kotarba, A.; Barański, A.; Hodorowicz, S.; Sokołowski, J.; Szytuła, A.; Holmlid, L. Stability and excitation of potassium promoter in iron catalysts—the role of KFeO<sub>2</sub> and KAlO<sub>2</sub> phases. *Catal. Lett.* **2000**, *67*, 129–134. [[CrossRef](#)]
65. Voronin, V.I.; Shekhtman, G.S.; Blatov, V.A. The natural tiling approach to cation conductivity in KAlO<sub>2</sub> polymorphs. *Acta Crystallogr. Sect. B Struct. Sci.* **2012**, *68*, 356–363. [[CrossRef](#)]
66. Peskov, M.V.; Schwingenschlög, U. First-principles determination of the K-conductivity pathways in KAlO<sub>2</sub>. *J. Phys. Chem. C* **2015**, *119*, 9092–9098. [[CrossRef](#)]
67. Demicheli, M.C.; Duprez, D.; Barbier, J.; Ferretti, O.; Ponzi, E. Deactivation of steam-reforming model catalysts by coke formation. II. Promotion with potassium and effect of water. *J. Catal.* **1994**, *145*, 437–449. [[CrossRef](#)]
68. Medina, F.; Salagre, P.; Sueiras, J.; Fierro, J. Surface characterization and catalytic properties of several graphite supported potassium-free and potassium-doped nickel catalysts. *Appl. Catal. A Gen.* **1993**, *99*, 115–129. [[CrossRef](#)]
69. Finetti, P.; Leatherman, G.; Caragiu, M.; Lindroos, M.; McGrath, R.; Diehl, R. Low-energy electron diffraction study of the surface geometry of Ni (100)–(3 × 3)–K+ 4O. *Surf. Sci.* **2000**, *462*, 77–84. [[CrossRef](#)]
70. Leininger, J.-P.; Lorant, F.; Minot, C.; Behar, F. Mechanisms of 1-methylnaphthalene pyrolysis in a batch reactor. *Energy Fuels* **2006**, *20*, 2518–2530. [[CrossRef](#)]
71. Pinilla, J.; Arcelus-Arrillaga, P.; Puron, H.; Millan, M. Reaction pathways of anthracene selective catalytic steam cracking using a NiK/Al<sub>2</sub>O<sub>3</sub> catalyst. *Fuel* **2013**, *109*, 303–308. [[CrossRef](#)]
72. Mohsenzadeh, A.; Bolton, K.; Richards, T. DFT study of the adsorption and dissociation of water on Ni (111), Ni (110) and Ni (100) surfaces. *Surf. Sci.* **2014**, *627*, 1–10. [[CrossRef](#)]
73. Xu, J.; Froment, G.F. Methane steam reforming, methanation and water-gas shift: I. Intrinsic kinetics. *AIChE J.* **1989**, *35*, 88–96. [[CrossRef](#)]
74. Do, L.T.; Nguyen-Huy, C.; Shin, E.W. Hierarchically ordered macro-mesoporous  $\gamma$ -alumina with a grainy wall structure. *J. Porous Mater.* **2016**, *23*, 1107–1112. [[CrossRef](#)]